Ultraslow waves on the nanoscale:
Slow light meets nanotechnology

Kosmas L. Tsakmakidis[1], Ortwin Hess[2], Robert W. Boyd[3], and Xiang Zhang[1,4]

[1]*NSF Nanoscale Science and Engineering Center (NSEC), University of California at Berkeley, 3112 Etcheverry Hall, Berkeley, CA, USA*
[2]*The Blackett Laboratory, Department of Physics, Imperial College London, London SW7 2AZ, United Kingdom*
[3]*Department of Physics and Max Planck Centre for Extreme and Quantum Photonics, University of Ottawa, Ottawa, Ontario K1N 6N5, Canada.*
[4]*Material Sciences Division, Lawrence Berkeley National Laboratory, 1 Cyclotron Road, Berkeley, California 94720, USA.*

There has recently been a surge of interest in the physics and applications of broadband ultraslow waves in nanoscale structures operating below the diffraction limit. They range from lightwaves or surface plasmons in nanoplasmonic devices to sound waves in acoustic-metamaterial waveguides, as well as fermions and phonon polaritons in graphene and van der Waals crystals and heterostructures. We review the underlying physics of these structures, which upend traditional wave-slowing approaches based on resonances or on periodic configurations above the diffraction limit. Light can now be tightly focused on the nanoscale at intensities up to ~1000 times larger than the output of incumbent near-field scanning optical microscopes, while exhibiting greatly boosted density of states and strong wave-matter interactions. We elucidate the general methodology by which broadband and, simultaneously, large wave-decelerations, well below the diffraction limit, can be obtained in the above interdisciplinary fields. We also highlight a range of applications for renewable energy, biosensing, quantum optics, high-density magnetic data-storage and nanoscale chemical mapping.

More than 100 years ago, in 1914, Sommerfeld, Brillouin and Lorentz started investigating situations where the group velocity v_g of light signals exceeds the vacuum speed of light, c, leading to what they initially thought were apparent inconsistencies with Einstein's special theory of relativity (*1-3*). The group velocity of a wavepacket propagating inside a dispersive medium of refractive index n is given by $v_g = c/n_g$, where $n_g = n + \omega(\mathrm{d}n/\mathrm{d}\omega)$ is the group refractive index of the medium, ω being the angular frequency, from where it is seen that in the region of anomalous dispersion in a normal absorbing medium, where $\mathrm{d}n/\mathrm{d}\omega < 0$, v_g may exceed c – but with high losses (*4-7*). More recently, experimental observations of superluminal group velocities have been reported in the propagation of mode-locked pulse trains in resonant absorbers (*8*) and in photon tunneling from potential barriers (*9, 10*). Furthermore, distortionless superluminal pulse propagation with minimal amplitude change has been observed in gain doublets (*11*), together with evanescent-wave superluminal group velocities at the cutoff of microwave waveguides (*12*), and superluminal effects arising solely from the nature of the propagating field, such as in the propagation of Bessel beams (*5, 13*). None of these situations violates relativistic causality as in all cases the front velocity, i.e. the velocity

with which a discontinuity in a waveform or one of its derivatives propagates, is smaller than c (*5, 9*).

The opposite phenomenon, where the group velocity of a lightwave can become much smaller than c, was also identified and studied (*3-6, 14*). For instance, within a hollow waveguide the wavevector β along the guide is reduced below the free-space value, leading to a phase velocity $v_\varphi = \omega/\beta$ greater than c. But within such a structure, the product of the phase and the group velocities is given as (*15*) $v_\varphi v_g = c^2$, thereby resulting in a group velocity along the guide that can become considerably smaller than c. A further intuitive example are epsilon-near-zero media (*16*), in which the electric permittivity $\varepsilon(\omega_0) \rightarrow 0$ at a frequency ω_0. In such media, the wavevector $k = (\omega/c)\sqrt{\varepsilon(\omega)}$ becomes zero at ω_0, hence the phase velocity v_φ becomes infinite, but the group velocity $v_g = (dk/d\omega)^{-1} = c[\sqrt{\varepsilon(\omega)} + \omega/(2\sqrt{\varepsilon(\omega)})]^{-1}$ becomes zero at $\omega = \omega_0$ (*17, 18*) – a property that can be exploited for boosting light-matter interactions and nonlinear effects (*16*).

Much of the impetus for the contemporary interest in such "slow" and "fast" light phenomena was the 1999 experiment (*19*) by Hau *et al.*, which demonstrated that the speed of light in atomic electromagnetically induced transparent (EIT) media could be reduced to the "human" scale of ~17 m/s – albeit over very narrow bandwidths (*20*), typically of the order of a few tens of kHz. Thereafter, a range of solid-state systems were proposed and investigated for slowing down the speed of guided light signals, including photonic crystal (PhC) waveguides (*21, 22*), coupled resonator optical waveguides (CROWs) (*23*) and standard optical fibers (*24, 25*). These slow-light structures exhibit fascinating fundamental physics and have allowed for a range of useful applications underpinned by the strong (and broadband) light-matter interactions that they entail (*26-28*). However, they are fundamentally limited by the wavelength of light, i.e. they are diffraction limited, and cannot reach true nanoscopic dimensions – e.g., scales less than around 30 nm.

More recently, media exhibiting negative electromagnetic/optical parameters (such as negative permittivity and/or refractive index) (*29-31*) have emerged as a new means of allowing large and broadband light decelerations – but, this time, well below the diffraction the limit, right at the nanoscale, where a host of new material properties, functionalities, applications and opportunities emerge. These media typically feature higher losses compared with their dielectric counterparts, thus one has to be mindful to target applications that can be more loss tolerant (*32, 33*). We will focus on wave-deceleration methods that allow – on the basis of the same underlying mechanisms in all cases – for simultaneously broadband operation and small group velocities, below the diffraction limit so that the nanoscale can be reached, in nanophotonic media, metamaterials, graphene, van der Walls crystals and heterostructures. We detail the broadband mechanisms, not involving bulk material-parameters (permittivity, refractive index) resonances, by which sub-diffraction waves of various kinds can be slowed-down in the aforementioned structures, their unique characteristics, and how these are exploited in a host of applications right across the fields of optics and photonics, acoustics and 2D condensed matter.

Physics of sub-diffraction slow and stopped lightwaves

Almost all types of nanoscale guiding structures inherently feature slow waves of some kind – light/photons, guided Dirac fermions, surface plasmon polaritons (SPPs) or surface phonon polaritons (SPhPs). This section reviews the physical mechanisms by which extremely slow light or SPPs can be obtained over broad spectral ranges below the diffraction limit, by exploiting suitably engineered and nanophotonic media.

Unlike atomic schemes (*19, 34, 35*) or periodic dielectric structures (*21-23, 26-28*), which are usually diffraction limited (*36, 37*), this route does not entail bulk-material resonances, disorder or periodic back-reflections to slow-down or stop light. The deceleration can occur even in longitudinally uniform (non-periodic) structures, and away from intrinsic material resonances – e.g., in a regime where the real part of the permittivity, ε, of a heterostructure's layer is negative, following a non-resonant Drude variation (*38*). Such structures can be either metamaterial or plasmonic waveguides (*38-62*) (Fig. 1, A to C). For transverse magnetic (TM) polarization, the time-averaged complex Poynting vector in the longitudinal z direction of a metamaterial waveguide (Fig. 1A), $\bar{S}_z$, is given by: $\bar{S}_z = \frac{1}{2}\mathrm{Re}\{\mathbf{E} \times \mathbf{H}^*\}_z = \frac{\beta}{2\omega\varepsilon_0\varepsilon_i}|H_y|^2$, where β is the longitudinal propagation constant, ε_i the layers' dielectric permittivities, and i = core layer or cladding layer (*42*). Thus, in the negative-permittivity (and negative-refractive-index) core layer of this symmetric, lossless waveguide it will be $\bar{S}_{z,\mathrm{co}} < 0$, while in the positive-permittivity dielectric cladding layers it will be $\bar{S}_{z,\mathrm{cl}} > 0$. Hence, the total time-averaged power flow, $P = \int_{-\infty}^{\infty}\bar{S}_z\,\mathrm{d}x$, in the $+z$ direction will be reduced owing to the negative contribution from $\bar{S}_{z,\mathrm{co}}$, and can even become zero when $|\bar{S}_{z,\mathrm{co}}| = 2\bar{S}_{z,\mathrm{cl}}$. But in a lossless dispersive medium (or waveguide) the energy velocity, v_E, is equal to the group velocity, v_g, and is given by $v_\mathrm{E} = P/U$, U being the energy density [*5, 6, 63*]. Therefore, as a result of the anti-parallel power flows in the core and cladding layers of this waveguide, both, its energy and group velocities can be reduced down to zero. As seen in Fig. 1A, the structure of the instantaneous Poynting vector $\mathbf{S}$ on the xz plane of the guide takes on a vortex form at each interface, with energy flowing back and forth across each interface but, on average, with no net energy being transported across each interface. Indeed, a straightforward calculation shows that the curl of $\mathbf{S}$, which characterizes it vorticity, is nonzero and is given by $\nabla \times \mathbf{S} = (\rho_s/\varepsilon_0)H_y\hat{\mathbf{y}}_0$, where ρ_s is the surface polarization charge density. Thus, the curl of the Poynting vector field is zero in, both, the negative-refractive-index core and dielectric cladding layers, and is nonzero (and maximum) only at the two interfaces, as inferred directly from Fig. 1A.

Figure 1B illustrates a further example of nanoscale light-slowing-down, this time in an adiabatically tapered plasmonic nanoguide (*40, 41*). Surface plasmon polaritons (SPPs) guided along this nanocone are progressively decelerated, until their group velocity becomes zero at the structure's tip where they accumulate (*40*). The SPPs are longitudinally and laterally compressed as they reach the tip, with the electric field being largely enhanced in that region, deep below the diffraction limit. Both of these nanoscale slow-light mechanisms – the double-vortex structure in the power flux vector, and the use of a tapered structure to accumulate light

in a sub-diffraction spot – underpin many of the underlying physics and applications that this type of light-deceleration features.

Slow light in these media is typically broadband, with Fig. 1C illustrating a tapered negative-index metamaterial waveguide capable of halting a "rainbow" of light wavelengths at pre-defined critical points (*42*). Here, a light ray is forced by the negative electromagnetic "environment" it experiences in the core layer of the guide to make, in each half period, a forward "step" followed by a negative phase-shift step. At the zero-group-velocity point the negative Goos-Hänchen phase-shifts bring the light ray precisely back to its initial position. The Goos-Hänchen phase shift arises when a finite-width beam (i.e., not a laterally infinitely-extended plane wave) is totally internally reflected at the interface of two media (e.g., from a high-, negative-permittivity ε medium "1" to a lower-, positive-permittivity medium "2", with $\varepsilon_1 < 0$ and $\varepsilon_2 > 0$, but with $|\varepsilon_1| > \varepsilon_2$) (*44, 45*). If κ is the component of the wavevector **k** perpendicular to the media interface, and γ the decay constant of the field into medium "2", then the Goos-Hänchen phase shift is given by $\delta = 2\tan^{-1}[(\varepsilon_1\gamma)/(\varepsilon_2\kappa)]$, and becomes negative for $\varepsilon_1 < 0$ (and $\varepsilon_2 > 0$) (*42*). This negative *phase* shift – an interference effect of multiple "plane waves" into which the incident beam can be analyzed, each impinging on the interface with a slightly different angle of incidence – gives rise to a negative (backwards) spatial displacement of the (center of the) beam, as shown schematically in the top insets of Fig. 1C. These backwards "steps" in the propagation of a light ray along the guide can also be understood by comparison with the negative (backwards) power flow in the core layer of the negative-index waveguide that we show before in Fig. 1A, and provide an intuitive, pictorial (yet accurate even at the level of Maxwell's equations) view of the herein attained light deceleration. These backwards Goos-Hänchen steps arise from the presence of a bulk, volume-averaged negative refractive index or permittivity in one or more of the layers. As a result, the effect of possible bulk disorders and fluctuations in the layers of the heterostructure is naturally averaged out (contained in the definition of the macroscopic effective refractive index or permittivity) (*29*). It is only the negativity in the real part of the effective refractive index or permittivity that enables the deceleration of light, even in uniform structures containing layers made of completely amorphous (meta)materials (*43*). The associated structures may also be longitudinally uniform plasmonic media, where disorder is not an inherent issue. Detailed studies have shown that in the presence of nm-scale surface roughness very large slow-down factors are still attainable – e.g., of the order of $\sim 10^7$ (*38*).

A universal characteristic of such negative-parameters wave-slowing structures – that one may also encounter for acoustic (*61, 62*) ultraslow-wave structures and 2D materials – is that they allow for field accumulation and significant field-enhancement around the critical light-stopping point, deep below the diffraction limit, which can be exploited for a host of nanoscale applications. This is contrast to, e.g., slow light in atomic media where although the energy density U is indeed enhanced in the slow-light regime ($U = P/v_g$, P being the power density, and $v_g \rightarrow 0$), the electric-field amplitude E is not enhanced because most of the compressed energy is stored in the atomic polarization – not in the electric field (*63*). Thus, although a light pulse is compressed in space (in the longitudinal direction of propagation) upon entering such an atomic ultraslow-light medium, and the energy density does increase, normally no enhancement is attained in the local electric field.

The situation is different in the sub-diffraction-limited nanophotonic structures considered herein. Assuming a parabolic-like v_g profile with distance (with $v_g = 0$ at the critical point), it is straightforward to show that the time it takes for the lightwave to exactly reach the critical point in an adiabatically tapered structure diverges logarithmically (*40, 64*); hence, that critical point (where $v_g = 0$) is, in theory, never reached because the effective optical distance, Ln_g, L being the guide's physical length, diverges ($n_g \rightarrow \infty$); it is as if a guided lightwave propagates towards one end of an infinitely-long waveguide (*65-67*), never quite reaching it. Accordingly, a sinusoidal light signal keeps accumulating, with a progressively smaller group velocity, near the "critical" zero-v_g point in this singular, idealized structure (Fig. 1, B and C). In practise, material imperfections lead to the critical point being reached, leading to a back-reflection, which together with material losses, provide a finite limit to how much the field can locally be enhanced. Still, the large spatial compression of the field in the slow-light regime of such sub-diffraction nanostructures leads to correspondingly large field-enhancement factors – of the order of 350 or more – being realistically attainable, and over ultrabroad bandwidths (e.g., FWHM of 100 nm in the near infrared) (*68*). Note that the back-reflection can be rigorously suppressed if non-reciprocity is broken, e.g. by application of a magnetic field in gyroelectric semiconductors (such as InSb) (*55, 56, 69*) or by deploying PT-symmetric structures (*58*), in which case rigorous light-stopping can be obtained. The ultimate degree of slow-light-aided field enhancement is set by the nonlocal effects in plasmonic structures and by the size of the unit cells in metamaterial structures (spatial dispersion), which set a limit to how much a lightfield can be spatially compressed (*70-72*). These nonlocal (spatial dispersion) effects usually arise at scales less than ~1-5 nm (~30-50 nm), and in that deep-subwavelength regime the induced spatial frequencies (i.e., wavevectors) are large, to the point of potentially allowing for "direct diagonal" *s*-band absorption (i.e., Landau damping) (*32*) – thereby potentially providing an additional loss channel that should be avoided. Such "structural slow-light" field-enhancements are also obtained in photonic structures above the diffraction limit, as in photonic crystals and coupled-resonator optical waveguides (*4-6, 21-28*). However, the compression and focusing of light in those cases is limited by the wavelength of light and cannot reach the truly nanoscopic dimensions (and corresponding nanoscale applications) targeted herein.

Robustness in the presence of dissipative and scattering channels

A key issue to be addressed when attempting to slow down or stop guided light signals in nanoscale structures is how dissipative losses (*38, 49-53*) and back-scattering channels (*54-56, 69*) might affect the light-deceleration ability of these devices. Because the light slowing-down arises due to the presence of negative electromagnetic parameters (Fig. 1, A to C), which normally entail losses and dispersion, the modes of these structures will in general be complex (*53*), and it is important to examine whether the zero-v_g points in the associated dispersion diagrams are still preserved when Joule losses are present. Furthermore, since the light-stopping points are usually reached and accessed using an adiabatic taper (Fig. 1, B and C), it is also crucial to check whether the taper might introduce back-scattering channels through which the trapped (stopped) light energy might escape.

Both of these issues have been extensively investigated and addressed. Exact solutions to Maxwell's equations in lossy plasmonic-dielectric-plasmonic heterostructures (*38*) reveal that there are two classes of modes in these structures (*38, 49-53*) (Fig. 2A). The first class is characterized by a real frequency *f* and complex longitudinal wavevector $\beta = \beta_r + i\beta_i$ (red and green lines in Fig. 2A), and do not preserve the zero-v_g points in the presence of losses (*49*). These modes can be excited by sinusoidal steady-state sources since they are characterized by a well-defined real frequency (and complex wavevector owing to the losses). They are not the modes to be sought-after in the stopped-light regime, since in that regime where light is trapped, spatial losses (complex wavevectors) lose their physical meaning (*53*) – a stopped light pulse simply decays with time at its localization point, rather than decaying in space (since it does not propagate); hence, spatial losses and the search for complex-β solutions cease to be physically meaningful in the stopped-light regime. The second class of modes, by contrast, is characterized by a complex frequency $f = f_r + if_i$ and real longitudinal wavevector β (blue lines in Fig. 2A) (*38, 51-53*). These "complex frequency" modes are somewhat similar to modes excited inside lossy cavity resonators, and are the ones to be sought-after in the stopped-light regime. They can be excited by short pulses that, e.g., have f_r as their central frequency and a bandwidth (*38*) $\Delta\omega = f_i$. Importantly, the temporal losses characterizing these modes only increase by a small factor when entering the stopped-light regime (e.g., from $\sim 2.4 \times 10^{13}$ s^{-1} at point "b" to $\sim 3.6 \times 10^{13}$ s^{-1} at the zero-v_g point "a" in Fig. 2A, an increase by a factor of only 0.5 – and corresponding to lifetimes at the stopping point of ~ 30 fs, which are typical nanoplasmonic ones) (*38, 51-53*).

To solve the second potential issue and supress back-scattering channels, a forceful way is to induce some kind of a unidirectionality mechanism, e.g. either by application of a static magnetic field in gyro-electric/-magnetic structures (*55, 56, 69*), nonlinear or refractive-index modulation mechanisms (*57*), PT-symmetric media (*58*) or photonic topological insulators (*59, 60*). For instance, we may see from Fig. 2B that the first of the aforementioned schemes, when applied to a (gyroelectric) semiconductor-dielectric-metal heterostructure, leads to a region in the band diagram where complete unidirectional propagation (CUP) is allowed. A guided pulse with a bandwidth falling inside this CUP region can neither scatter to backwards modes ($k < 0$ in Fig. 2B) nor to bulk modes in the semiconductor (orange-coloured regions in Fig. 2B) nor to surface waves (SWs) at the semiconductor-metal interface of a metal-terminated such waveguide – neither can it be perturbed by surface roughness and geometric imperfections, being a photonic analogue of a quantum Hall state (*55, 69*). Thus, with such unidirectional schemes supressing back-scattering channels, robust slow and stopped light can be attained, unharmed by spatial variations in the guiding structure.

Applications of sub-diffraction ultraslow light and acoustic waves

An example of such a broadband ultraslow-light effect, below the diffraction limit, and its application is illustrated in Fig. 1D, where an adiabatically tapered plasmonic nanoguide capable of decelerating and accumulating at its tip surface plasmon polaritons (SPPs) over a broad band (~ 100 nm) (cf. Fig. 1B) is used as a means of generating ultrashort, extreme-ultraviolet (EUV) pulses from near-infrared incident pulses (centered ~ 800 nm) (*68*). The SPPs in this tapered hollow nanocone are dramatically slowed-down near its exit point, accumulating

in an area with diameter of approximately 240 nm. Atomic gases enter the device at the input port, and are controlled by changing the pressure between the input and output ports. Despite the plasmonic losses, optimized structures lead to intensity-enhancements exceeding 20 dB (i.e., a factor of ~350), enough to trigger atomic ionization with moderate input intensities of ~1×10^{11} W cm^{-2}. This leads to high-harmonic generation, up to the 43rd harmonic (Fig. 1D), and deep into the UV regime (photon energy ~67 eV). In addition to not requiring phase-matching, as the field concentration is deep-subwavelength, an advantage of this means of nano-localizing and enhancing the intensity of light compared to bowtie or nano-rod elements is that the large field-enhancements occur over significantly larger nano-volumes (having here a diameter of ~240 nm and a length of ~ 450 nm), thereby enhancing the efficiency of the nonlinear generation. For instance, the photon number measured for the 15th and 17th harmonics was ~1×10^{9} photons/s, corresponding to a conversion efficiency of ~1×10^{-8}, which is about 10-100 times higher than that measured for a 150-bowtie-nanoantenna array (*73*). We note that under similar conditions non-coherent multi-photon or high-field fluorescence may also dominate the spectra (*74*), since these effects too are favored below the ionization threshold by the large field-enhancements and the linear interaction length scaling.

This type of broadband slow-light structures need not be planar (*38, 65-67*) nor linearly tapered (*40-42, 73-82*), with two examples being the cylindrically (*64*) or spherically (*83*) crescent nanostructures (Fig. 1E and Fig. 3). Surface plasmon modes excited by a uniform electric field of wavelength λ ~375 nm travel with a gradually slower speed towards the singular "kissing" point of the two cylinders (of external radius ~20 nm) where they accumulate, having a gradually smaller wavelength and increased energy density (Fig. 1E). On the basis of a transformation-optics analytic approach, it was shown that this effect is ultra-broadband – across the entire visible spectrum – and, despite the plasmonic loss, leads to large field-enhancements, of the order of 10^{3}, at the critical stopping point (*64*). The role of surface roughness and unavoidable geometric bluntness and imperfections has also been studied in refs. (*84, 85*), and it was found that the structures' fundamental behaviour remained unaltered. We note that reported in the pertinent literature have been similar plasmonic nanostructures with, even, sub-nm defined features – in the regime where nonlocal effects start playing a dominant role (*70-72*).

In an example of how such a broadband slow-light-aided field-enhancement can be exploited to improve the performance of photovoltaic solar cells (Fig. 3A), a layer containing spherical nano-crescents composed of an upconverter-doped dielectric core and a crescent-shaped metallic shell is placed behind the solar cell (*86*), capable of transforming over broad spectral and spatial regions transmitted low-energy photons to higher-energy, above-bandgap photons that can be absorbed by the solar cell. Based on detailed calculations, a 100-fold increase in above-bandgap power emission towards the solar cell was reported (*86*), and a greater than 10-fold absorption enhancement for a broad range of sub-bandgap wavelengths (Fig. 3, B and C) – leading to calculated single-junction solar cell power-conversion efficiencies that can exceed the Shockley-Queisser limit (from ~30% to over 44%). We note that in such nano-engineered structures one has the ability to exploit broadband slow-light and large near-field intensity-enhancement effects right at the meta-atomic level, i.e. not only the macroscopic overall structure but even its constituent meta-molecules (nanoantennas) can be

designed to harness broadband slow light – a unique feature compared with other macroscopic slow-light-structure designs.

These slow-light "nanocrescent-moon" meta-molecules can also be used as an ultra-sensitive surface-enhanced Raman scattering (SERS) substrate (Fig. 3D) (87). The gold nanocrescents (300 nm inner diameter and 100 nm bottom thickness) are functionalized with biomolecular linkers to identify specific biomolecules. When a single gold nanocrescent moon is excited by a 785 nm diode laser, the generated broadband hot-spot is utilized to detect the SERS spectra of Rhodamine 6G (R6G) molecules, with an enhancement factor larger than 10^{10}. Comparing the SERS spectra of 1 mM R6G molecules on a single gold nanocrescent moon and on 60 nm colloidal nanospheres (Fig. 3E) shows substantial improvement by the use of the former structure – both, in the number and the relative intensity of the resolved Raman peaks. These broadband slow-light nanophotonic crescent moons exhibit Raman enhancement factors (for a 830 nm laser excitation source) exceeding 10^{10}, as compared with 10^3-10^4 corresponding factors for on-resonance Au nanospheres (using 514 nm laser excitation) reported previously (88).

The broadband field-enhancement in the ultraslow-light regime of tapered metamaterial and nanoplasmonic waveguides has been exploited in a variety of further applications, including broadband thin-film infrared absorbers (89), spontaneous-emission enhancement of single quantum dots and nonclassical light sources (90), cavity-free stopped-light nanolasing and active on-chip nanophotonic devices (36, 91-94). However, quite a few of the reported three-dimensional sub-diffraction slow-light structures, such as the linearly-tapered cylindrical nanoguides of Fig. 1, B and D, are stand-alone devices, with their on-chip implementation being challenging. A first quantitative study towards overcoming this issue was reported in ref. (80), which demonstrated nanoscale two-dimensional slowing of light in the form of SPPs (Fig. 4, A to C). Here, light was adiabatically slowed-down and squeezed (with an efficiency of ~50%) through a 45 nm × 2 μm V-groove slit aperture, resulting in a measured intensity enhancement of ~10 – the defining feature of, so called, "structural slow light" (4-6) in guiding structures, both below and above the diffraction limit. The full extension of this nanoscale slow-light scheme to three dimensions was reported recently (95), giving rise to experimentally estimated intensity enhancements of ~400 within a mere 14×80 nm^2 cross-sectional area, and allowing for efficient on-chip slow light that can be readily integrated with other on-chip nanophotonic components. The attained spatial compression achieved in the slow-light regime of plasmonic slot nanoguides was exploited in ref. (95) to reduce the length and overall footprint of a plasmonic electro-optic phase modulator, giving rise to large bandwidths (~120 nm around 1.55 μm), high modulation speeds (~40 Gbit s^{-1}), compactness (length of only ~29 μm and a width of ~140 nm), and energy-efficient operation (energy consumption ~60 fJ bit^{-1}).

This type of ultra-broadband light-deceleration can be attained in almost any regime of the electromagnetic spectrum, from microwaves (66, 67) to the THz (55, 75, 77), near-infrared (76) and visible regime (78-82, 97, 98), using suitably engineered plasmonic structures. Two examples of this are shown in Fig. 4, D (theory, at telecommunication wavelengths (76)) and E (experiment, at visible wavelengths (97)). In particular, Fig. 4E shows so-called "spoof" (engineered) surface plasmon polaritons (SPPs) being excited at a nanoslit (extending horizontally, from left to right, in the upper panels of the figure, perpendicularly to the arrows)

and propagating along the direction of the arrows. The SPPs propagate along a tapered plasmonic grating structure, similar to that discerned in Fig. 4D, in the direction indicated by the arrows. In this adiabatically tapered structure, the period and the width of the grooves are fixed (approximately 475 and 150 nm, respectively) but the groove depth increases with distance slowly from approximately 6 nm to 100 nm. As they propagate along the adiabatically tapered structure, the SPPs (in the visible wavelength region, 500-700 nm) disperse, with each visible color eventually being trapped and localizing at a correspondingly different point along the tapered structure – with the larger (red) wavelengths localizing at the deepest grooves. These experimental results, therefore, provide confirmation in the visible regime of the spatial demultiplexing and trapping at different positions of the spectrum of a broadband pulse ("rainbow trapping") propagating along a tapered plasmonic waveguide – similar to the effect outlined theoretically before in Fig. 1, B and C, for tapered plasmonic and negative-index waveguides, respectively. The resulting spectrum demultiplexing can, in this scheme, find interesting applications for on-chip spectroscopy (*82*), filtering and color sorting (*78, 99*).

Being essentially an interference phenomenon (Fig. 1, A and C), the wave deceleration in adiabatically tapered metamaterial waveguides can also be exploited for acoustic waves (*61, 62*). Here, the concept of meta-materials (judiciously engineered media with desired wave responses) is especially fitting as it allows to design – in the deep-subwavelength, true-effective-medium regime – structures with broadband slow-wave acoustic responses unattainable with natural media. An example is illustrated in Fig. 5, A to D. Here, a tapered acoustic metamaterial waveguide brings an input pressure field (sound wave) to a halt at a critical point inside the waveguide, where the acoustic field can now build-up and be locally enhanced (cf. Fig. 1, B and C, for the photonic analogue), so that it can be detected with ultrahigh sensitivity by an acoustic sensor at the guide's end (Fig. 5A) (*61*). The acoustic-metamaterial device is constructed by an array of stainless plates, spaced by air gaps, and behaves as a continuous medium. Excited by a speaker, the acoustic wave (of frequency ~ 7 kHz) propagates with a progressively slower speed along the structure, and is therefore spatially compressed and enhanced in amplitude, until it is eventually detected at its stopping point by a fiber-optic microphone integrated at the wide, open end of the device (Fig. 5B). More than tenfold pressure amplification is achieved in this way. The broadband acoustic-wave enhancement in this type of a system is in fact so large that it can be used to successfully recover very weak acoustic-pulse signals far *below* the detection limit of conventional acoustic-sensing systems. Figure 5, C to D, shows how a series of Gaussian-modulated acoustic pulses with a center frequency of 9.3 kHz and a bandwidth of 0.5 kHz are effectively amplified in the slow-wave acoustic-metamaterial device, with an achieved signal-to-noise ratio (SNR) enhanced by more than 100 times (that is, more than 20 dB) compared with that obtained in free space. This SNR enhancement, enabled the metamaterial slow-wave system to detect weak acoustic signals below the detection limit of a conventional acoustic sensor: Indeed, we see from Fig. 5D (top) that while the measured free-space signal is completely overwhelmed by the noise (that is, SNR = 0.27), the same weak acoustic pulse is successfully recovered (that is, SNR = 32.7) in the slow-wave metamaterial region (Fig. 5D, bottom).

Finally, Fig. 5, E to G, highlights what we believe is one of the most exciting and technologically promising applications of slow-light-aided nanoscale field-enhancement: heat-assisted magnetic recording (HAMR) for data storage. Since 2012, the density growth rate of

hard disk drives (HDDs) has begun saturating due to fundamental physical limits reached by perpendicular magnetic recording – in particular, owing to the fact that the required writing field in HDD electromagnets has to be higher than that of the magnetic flux saturation in a typical CoFe based electromagnet (*100*). A promising avenue that the industry is currently pursing to overcome this limitation is HAMR, which exploits the sudden drop of a magnet's coercivity at the critical Curie temperature. To achieve the required high local heating (~400° C), typically ~80 μW of laser light from an inexpensive semiconductor diode (operating at ~830 nm, although with blue-ray laser diodes it can be at ~ 400 nm) need to be efficiently brought to the nanoscale to heat (from a distance of only ~5 nm above the recording head) a volume of ~50×15×10 nm^3 of a FePt ferromagnet. To put this into a context, the required power density for HAMR is approximately one thousand times larger than that resulting from standard Au-coated tapered optical fibers used in near-field scanning optical microscopy (NSOM), which typically have an optical transmission efficiency of less than 10^{-5}. Figures 5, E and F, show an example, reported in 2009 by Seagate Technology, of how slow-light nanoguides can be used in a HAMR recording head to solve the above challenges (*101*). Here, diode-laser light at 830 nm is coupled to a gold-coated parabolically-tapered Ta_2O_5 slab. As it propagates along the metal-clad tapered waveguide (*44*), the light signal is gradually decelerated, spatially compressed, and enhanced in amplitude, until it reaches the guide's cutoff thickness where it momentarily stops ($v_g = 0$ at the cutoff (*44*)) – a behaviour fundamentally similar (*64, 83-85*) to what was described before for the structures of Figs. 1 and 3, the only difference now being that the taper is not linear (Fig. 1, B and D), cylindrical (Fig. 1E) or spherical (Fig. 3, A and D) but parabolic. It then evanescently couples with good efficiency to a gold nanoantenna, producing an intense localized field, well below the diffraction limit, and only a few nm above the hard disk – enough to induce the required local heating. For optimized structures, the authors of ref. (*101*) reported maximum field-enhancements of ~2000, and a maximum coupling efficiency (at ~870 nm) of ~8% – orders of magnitude greater than the coupling efficiency of conventional apertures with diameters of the same dimensions as the nanoantenna. This method has thereby allowed for locally heating an only ~70 nm-wide magnetic track (Fig. 5G), giving rise to a data-recording areal density of ~375 Tb m^{-2} – much higher than previously reported storage densities (*100, 101*). Important remaining challenges for this technique concern the efficient integration of materials that will be even more resilient to thermal damage (upon repeated heating cycles), more efficient heat sinks and dedicated nm-gap-regulation techniques between the writing head and the recoding disk.

Broadband ultraslow electron and phonon-polariton waves in 2D materials

The non-resonant mechanisms for the deceleration of guided lightwaves in nanostructures containing media with negative optical parameters that we reviewed previously (Fig. 1, A to C) play also a critical role in the slowing-down of electron and phonon-polariton waves in two-dimensional nanoguides and heterostructures. Here, an additional advantage is the convenience with which one can control the velocity of guided matter waves, e.g. by smoothly varying a gate voltage applied on a 2D graphene quantum-well structure, thereby allowing for the possibility of variable delays – an important aspect of coherent buffers and memories (*4-6*).

The quantum Goos-Hänchen effect in the ultra-relativistic limit of massless electrons, relevant for graphene, considered the propagation of massless spin-1/2 particles in two dimensions, in a *p-n-p* single-layer graphene junction with a voltage (potential barrier) U_0 applied in the *p*-doped regions (*102*) (Fig. 6A, upper panel). It was found that the Goos-Hänchen effect at the *p-n* interfaces depends on the pseudospin (sublattice) degree of freedom of the massless Dirac fermions, and – importantly – that it changes sign at an angle of incidence $\alpha_s = \arcsin\{(\sin\alpha_c)^{1/2}\}$, α_c being the critical angle for total reflection, for Fermi energies $E_F < U_0$. For angles of incidence smaller than α_s, the shift becomes negative (Fig. 6A, lower panel), just as with guided lightwaves in metamaterial and plasmonic waveguides that we show previously in Fig. 1C. In that regime, the group velocity v of the guided quasiparticles can become zero. In particular, as the normalised width ($U_0 W/\hbar v$) of the central *n*-doped channel is progressively reduced to around unity, i.e. as one enters the full quantum-mechanical regime, the dispersion relation of the lowest channel-mode features two pronounced minima (where the group velocity reduces to zero, $v = 0$), each contributing to the conductance a quantum of $e^2/\hbar$ per spin and valley degree of freedom, thereby making a total contribution to the conductance of $8e^2/\hbar$ – a macroscopic conductance step that is observable in these bipolar junctions. Similar effects can be observed in bilayer graphene junctions, too, where it is possible to coherently decelerate, stop and re-accelerate the guided quasiparticles, allowing for interesting coherent-manipulation functionalities in graphene based integrated devices (*103*).

In addition to slowly-propagating guided Dirac fermions in doped graphene slots of suitable geometry, there is currently a significant interest in the interaction of infrared light with Dirac plasmons or phonons, particularly in the slow-wave regime of these nanostructures. In that regime, the longitudinal wavevector of the guided wave is large and the effective wavelength small, leading to volume confinements that can be millions of times smaller than in free space, with relatively low losses – thereby allowing for ultrastrong light-matter interactions. An interesting example of this is illustrated in Fig. 6B, showing a graphene sheet encapsulated by two films of hexagonal boron nitride (h-BN) – the whole structure assembled by a polymer-free van der Waals (vdW) assembly technique (*104, 105*). Hexagonal boron nitride is in itself an interesting optical material for nanoscale slow-light applications as it exhibits natural hyperbolic behaviour (*106*), i.e. the in- and out-of-plane components of the permittivity tensor have opposite signs in the reststrahlen frequency bands. Fig. 6C presents the dispersion diagram (energy/wavelength vs. wavevector) of propagating Dirac plasmon modes in the structure shown in Fig. 6B. In Fig. 6C, the crosses are the experimentally extracted data, indicating group velocities $v_g = (\mathrm{d}\,\mathrm{Re}q_{\mathbf{p}}/\mathrm{d}\omega)^{-1}$, $q_{\mathbf{p}}$ being the plasmon wavevector, as small as ~10^6 m s^{-1} (group refractive index ~300), and corresponding to observed lifetimes (not shown directly in this figure), $\tau_{\mathbf{p}} = (\mathrm{Im}\,q_{\mathbf{p}})^{-1}/v_g$, as long as ~500 fs (*104*) – more than an order-of-magnitude longer than those of pure surface plasmons in silver, which are typically ~20 fs (*48*). Furthermore, the wavelength $\lambda_{\mathbf{p}}$ of the Dirac plasmons is as low as 70 nm – some 150 times smaller than the free-space wavelength of the incident light. With an even further improvement of these plasmons' lifetimes, such a structure should be ideal for slow-wave applications where ultrahigh field confinement and tunability are desirable (*104, 107*), particularly for achieving low-threshold single-plasmon (photon) nonlinearities (*108*).

Still larger propagation lengths, in atomic van der Waals crystals (e.g., h-BN), can be achieved when light couples to pure optical phonons, giving rise to slowly-propagating phonon

polaritons. In this case, one of the dominant loss channels, electronic losses, is absent. This leads to propagation lengths of up to 50 μm (for incident free-space wavelengths $\lambda_0 \sim$5-6 μm), as compared to $\sim$2 μm (for a typical $\lambda_0 \sim$10 μm) in graphene (*107*). Figure 6D illustrates how ultraslow negative-phase-velocity phonon polaritons are excited and detected in a thin h-BN waveguide exhibiting hyperbolic dispersion and deep subwavelength-scale field confinement (*110*). Owing to its layered crystal structure, h-BN is a natural material in which phonon polaritons exhibiting hyperbolic dispersion exist – and there are two types of guided slow modes: type I, when Re$\{\varepsilon_z\} < 0$ and Re$\{\varepsilon_x\} > 0$; and type II, when Re$\{\varepsilon_z\} > 0$ and Re$\{\varepsilon_x\} < 0$. Here, incident infrared light (from free space; see Fig. 6D) of frequency $\omega = 1{,}563$ cm^{-1} ($\lambda \sim$6.4 μm) couples to and excites guided hyperbolic polariton modes in the h-BN slab, whose transverse (along z) spatial profile is shown in the right panel of Fig. 6E. Specifically, the Au film shown in this figure serves as a broadband optical antenna, converting the incident *p*-polarized field (E_in) into strongly spatially confined (high momentum) near fields at the film's rightmost edge, thereby providing the necessary momentum for coupling the free-space E_in field into the guided modes of the h-BN slab. Based on time-domain interferometric and scattering-type near-field microscopy measurements (Fig. 6, D and F), it was found that the group velocity of the fundamental type-I mode was as small as $\sim$0.002c (group index $\sim$500) and with a large lifetime of $\sim$1.8 ps – more than an order of magnitude larger than that of SPPs in Au at visible frequencies. Furthermore, the phase velocity of this mode was found to be negative (antiparallel to the forward-longitudinal direction of the group velocity) (*110*). Both of these results were found to be in excellent agreement with theory (see, e.g., Fig. 6G). We note that, at the moment, the operation of these structures is constrained at longer (infrared) wavelengths and it is challenging to be pushed into the visible regime. Furthermore, in these "phononic" materials most of the energy is stored in the kinetic and potential energy of the oscillating ions – and not so much in the electric field –(*32*), which sets a limit to the maximum field-enhancements attained.

Conclusions and outlook

We have examined the underlying physical principles enabling broadband*,* ultraslow waves in sub-diffraction-limited nanostructures, and we presented exemplary technological applications in the fields of nanophotonics, metamaterials, acoustics and 2D materials. The deployed structures are usually geometrically smoothly-varying (Fig. 1B) and the underlying wave-deceleration mechanisms inherently do not involve material-parameters (permittivity, refractive index) resonances – typically relying on anti-parallel power flows in the negative- and positive-permittivity regions (Fig. 1A) or, equivalently, to negative Goos-Hänchen phase shifts at the interfaces of these media (Fig. 1C). Ultimately, material and group-velocity dispersion set a limit to the attained bandwidth performance (*25, 63*). However, it should be noted that the so-attained bandwidths in the considered structures can still, in the optical regime, be large, typically of the order of $\sim$1-10 THz – orders of magnitude larger than, e.g., their atomic-media counterparts (which feature similar order-of-magnitude decelerations). Furthermore, upon suitable design, e.g. in multilayer heterostructures, the dispersion band can (for a continuous range of wavevectors) become very flat, i.e. group-velocity dispersion can be minimized (*38*) – thereby leading to enhanced bandwidth performance. This last feature – that

the bandwidth can be enhanced and engineered "by design" at the nanoscale – is a key characteristic of the herein reviewed (ultra)slow-light structures.

Specific applications range from enhanced and more efficient nonlinear effects (*68*, *73*, *74*, *108*), to light-harvesting (*64*, *83*, *89*), bio-sensing (*87*, *88*), nano-imaging (*80*, *111*), optical and acoustic spectral demultiplexing (*40-42*, *55*, *56*, *61*, *62*, *64*, *68*, *75-81*), on-chip spectroscopy (*82*), non-classical light sources (*90*, *91*), cavity-free plasmonic nanolasing (*92-94*), enhanced acoustic sensors operating beyond the noise-threshold limit (*61*, *62*), and tunable, deep-subwavelength, ultraslow guided Dirac fermions (*102*, *103*), plasmons and surface phonon-polaritons in atomically-thin crystals and heterostructures (*104-110*). Broadband slow-light effects are also attained in other structures above the diffraction-limit, including photonic crystals and CROWs where broadband slow light is usually obtained with group indices of ~30-100 (*21-28*), and PT-symmetric structures, which can be broadband and with the light speed reducing to zero at the exceptional point (*58*, *114*). Further related schemes include broadband metamaterial and nanophotonic analogues of EIT (*115*), or suitably engineered metasurfaces to induce negative Goos-Hänchen phase shifts and achieve the same light-stopping effect but without the use of bulk negative-parameters media (*116-118*).

The broadband, ultraslow-wave regime in sub-diffraction-limited nanostructures is essentially a new regime for nanophotonics, acoustics and 2D materials, as in all three fields we have been accustomed to using fast, propagating waves for diverse operations and devices. Many surprises are awaiting to be exhumed and even further exciting applications to emerge in the future in this new regime.

REFERENCES AND NOTES

1. A. Sommerfeld, Über die fortpflanzung des lichtes in dispergierenden medien. *Ann. Phys*. **44**, 177-202 (1914); English translation available in L. Brillouin, *Wave Propagation and Group Velocity* Ch. II (Academic, New York, 1960).
2. L. Brillouin, Über die fortpflanzung des lichtes in dispergierenden medien. *Ann. Phys*. **44**, 203-240 (1914); English translation available in Brillouin, L. *Wave Propagation and Group Velocity* Ch. III (Academic, New York, 1960).
3. H. A. Lorentz, Uber die Beziehung zwischen der Fortpflanzung des Lichtes und der Körperdichte. *Wiedemann Ann*. **9**, 641–664 (1880).

4. R. W. Boyd, D. J. Gauthier, Slow and fast light. *Prog. Optics* **43**, 497–530 (2002).

5. P. W. Milonni, *Fast Light, Slow Light, and Left-handed Light* (Institute of Physics, 2005).

6. J. B. Khurgin, R. S. Tucker, *Slow Light: Science and Applications* (Taylor & Francis, 2009).

7. S. Chu, S. Wong, Linear pulse propagation in an absorbing medium. *Phys. Rev. Lett.* **48**, 738 (1982).

8. F. R. Faxvog, C. N. Y. Chow, T. Bieber, J. A. Carruthers, Measured pulse velocity greater than *c* in a neon absorption cell. *Appl. Phys. Lett.* **17**, 192-193 (1970).

9. R. Y. Chiao, A. M. Steinberg, Tunneling times and superluminality. *Prog. Opt.* **37**, 345-405 (1997).

10. H. G. Winful, Nature of "superluminal" barrier tunneling. *Phys. Rev. Lett.* **90**, 023901 (2003).

11. L. J. Wang, A. Kuzmich, A. Dogariu, Gain assisted superluminal light propagation. *Nature* **406**, 277-279 (2000).

12. G. Nimtz, W. Heitmann, Superluminal photonic tunneling and quantum electronics. *Prog. Quantum Electron.* **21**, 81-108 (1997).

13. J. Durnin, J. J. Miceli, Jr., J. H. Eberly, Diffraction-free beams. *Phys. Rev. Lett.* **58**, 1499-1501 (1987).

14. R. W. Boyd, D. J. Gauthier, Controlling the velocity of light pulses. *Science* **326**, 1074 (2009).

15. D. Giovannini *et al.*, Spatially structured photons that travel in free space slower than the speed of light. *Science* **347**, 857 (2015).

16. I. Liberal, N. Engheta, Near-zero refractive index photonics. *Nature Photon.* **11**, 149-158 (2017).

17. A. Ciattoni, A. Marini, C. Rizza, M. Scalora, F. Biancalana, Polariton excitation in epsilon-near-zero slabs: Transient trapping of slow light. *Phys. Rev. A* **87**, 053853 (2013).

18. M. H. Javani, M. I. Stockman, Real and imaginary properties of epsilon-near-zero materials. *Phys. Rev. Lett.* **117**, 107404 (2016).

19. L. V. Hau, S. E. Harris, Z. Dutton, C. H. Behroozi, Light speed reduction to 17 metres per second in an ultracold atomic gas. *Nature* **397**, 594–598 (1999).

20. M. Klein *et al.*, Slow light in narrow paraffin-coated vapor cells. *Appl. Phys. Lett.* **95**, 091102 (2009).

21. T. Baba, Slow light in photonic crystals. *Nature Photon.* **2**, 465–473 (2008).

22. Y. A. Vlasov, M. O'Boyle, H. F. Hamann, S. J. McNab, Active control of slow light on a chip with photonic crystal waveguides. *Nature* **438**, 65-69 (2005).

23. A. Yariv, Y. Xu, R. K. Lee, A. Scherer, Coupled-resonator optical waveguide: a proposal and analysis. *Opt. Lett.* **24**, 711–713 (1999).

24. Z. Zhu, D. J. Gauthier, R. W. Boyd, Stored light in an optical fibre via stimulated Brillouin scattering. *Science* **318**, 1748–1750 (2007).

25. J. T. Mok, C. M. De Sterke, I. C. M. Littler, B. J. Eggleton, Dispersionless slow light using gap solitons. *Nature Phys.* **2**, 775-780 (2006).

26. B. Corcoran *et al.*, Green light emission in silicon through slow-light enhanced third-harmonic generation in photonic-crystal waveguides. *Nature Photonics* **3**, 206-210 (2009).

27. M. Soljačić, S. G. Johnson, S. Fan, M. Ibanescu, E. Ippen, J. D. Joannopoulos, Photonic-crystal slow-light enhancement of nonlinear phase sensitivity. *J. Opt. Soc. Am. B* **19**, 2052–2059 (2002).

28. P. Markoš, C. M. Soukoulis, *Wave Propagation: From Electrons to Photonic Crystals and Left-Handed Materials* (Princeton Univ. Press, 2008).

29. R. Marqués, F. Martín, M. Sorolla, *Metamaterials with Negative Parameters: Theory, Design and Microwave Applications* (Wiley, 2013).

30. W. Cai, V. M. Shalaev, *Optical Metamaterials: Fundamentals and Applications* (Springer, 2010).

31. S. Bozhevolnyi, *Plasmonic Nanoguides and Circuits* (Pan Stanford, 2008).

32. J. B. Khurgin, How to deal with the loss in plasmonics and metamaterials. *Nature Nanotechnol.* **10**, 2-6 (2015).

33. S. I. Bozhevolnyi, J. B. Khurgin, The case for quantum plasmonics. *Nature Photon.* **11**, 398-400 (2017).

34. S. E. Harris, Electromagnetically induced transparency. *Phys. Today* **50**, 36–42 (1997).

35. M. D. Lukin, A. Imamoğlu, Controlling photons using electromagnetically induced transparency. *Nature* **413**, 273–276 (2001).

36. O. Hess, J. B. Pendry, S. A. Maier, R. F. Oulton, J. M. Hamm, K. L. Tsakmakidis, Active nanoplasmonic metamaterials. *Nature Materials* **11**, 573-584 (2012).

37. M. S. Tame, K. R. McEnery, Ş. K. Özdemir, J. Lee, S. A. Maier, M. S. Kim, Quantum Plasmonics. *Nature Physics* **9**, 329-340 (2013).

38. K. L. Tsakmakidis *et al*., Completely stopped and dispersionless light in plasmonic waveguides. *Phys. Rev. Lett*. **112**, 167401 (2014).

39. I. V. Shadrivov, A. A. Sukhorukov, Y. S. Kivshar, Guided modes in negative-refractive-index waveguides. *Phys. Rev. E* **67**, 057602 (2003).

40. M. I. Stockman, Nanofocusing of optical energy in tapered plasmonic waveguides. *Phys. Rev. Lett*. **93**, 137404 (2004).

41. K. V. Nerkararyan, Superfocusing of a surface polariton in a wedge-like structure," *Phys. Lett*. A **237**, 103-105 (1997).

42. K. L. Tsakmakidis, A. D. Boardman, O. Hess, "Trapped rainbow" storage of light in metamaterials. *Nature* **450**, 397–401 (2007).

43. C. Helgert *et al*., Effective properties of amorphous metamaterials. *Phys. Rev. B* **79**, 233107 (2009).

44. M. J. Adams, *An introduction to Optical Waveguides* (Wiley, 1981).

45. A. H. Cherin, *Introduction to Optical Fibers* (McGraw-Hill, 1982).

46. K. L. Tsakmakidis, A. Klaedtke, D. P. Aryal, C. Jamois, O. Hess, Single-mode operation in the slow-light regime using oscillatory waves in generalized left-handed heterostructures. *Appl. Phys. Lett.* **89**, 201103 (2006).

47. K. L. Tsakmakidis, C. Hermann, A. Klaedtke, C. Jamois, O. Hess, Surface plasmon polaritons in generalized slab heterostructures with negative permittivity and permeability. *Phys. Rev. B* **73**, 085104 (2006).

48. L. Novotny, B. Hecht, *Principles of Nano-optics* (Cambridge Univ. Press, 2012).

49. A. Reza, M. M. Dignam, S. Hughes, Can light be stopped in realistic metamaterials? *Nature* **455**, E10-E11 (2008).

50. K. L. Tsakmakidis, A. D. Boardman, O. Hess, Can light be stopped in realistic metamaterials? *Nature* **455**, E11-E12 (2008).

51. A. Archambault, T. V. Teperik, F. Marquier, J. J. Greffet, Surface plasmon Fourier optics. *Phys. Rev. B* **79**, 195414 (2009).

52. A. Archambault, M. Besbes, J. J. Greffet, Superlens in the time domain. *Phys. Rev. Lett*. **109**, 097405 (2012).

53. K. C. Huang *et al*., Nature of lossy Bloch states in polaritonic photonic crystals. *Phys. Rev. B* **69**, 195111 (2004).

54. S. He, Y. He, Y. Jin, Revealing the truth about 'trapped rainbow' storage of light in metamaterials. *Sci. Rep*. **2**, doi:10.1038/srep00583 (2012).

55. L. Shen, X. Zheng, X. Deng, Stopping terahertz radiation without backscattering over a broad band. *Opt. Express* **23**, 11790 (2015).

56. K. Liu, S. He, Truly trapped rainbow by utilizing nonreciprocal waveguides, *Sci. Rep*. **6**, doi:10.1038/srep30206 (2016).

57. D. Jalas *et al*., What is – and what is not – an optical isolator. *Nature Photonics* **7**, 579-582 (2013).

58. C. E. Rüter *et al*., Observation of parity-time symmetry in optics. *Nature Physics* **6**, 192-195 (2010).

59. M. C. Rechtsman *et al*., Photonic Floquet topological insulators. *Nature* **496**, 196-200 (2013).

60. A. B. Khanikaev *et al*., Photonic topological insulators. *Nature Materials* **12**, 233-239 (2013).

61. Y. Chen, H. Liu, M. Reilly, H. Bae, M. Yu, Enhanced acoustic sensing through wave compression and pressure amplification in anisotropic metamaterials. *Nature Commun*. **5**, 5247 (2014); doi:10.1038/ncomms6247

62. J. Zhu *et al*., Acoustic rainbow trapping. *Scientific Reports* **3**, 1728 (2013); doi:10.1038/srep01728

63. J. B. Khurgin, Slow light in various media: a tutorial. *Adv. Opt. Photon*. **2**, 287-318 (2010).

64. A. Aubry *et al*., Plasmonic light-harvesting devices over the whole visible spectrum. *Nano Lett*. **10**, 2574-2579 (2010).

65. W. T. Lu, Y. J. Huang, B. D. F. Casse, R. K. Banyal, S. Sridhar, Storing light in active optical waveguides with single-negative materials. *Appl. Phys. Lett.* **96**, 211112 (2010).

66. W. T. Lu, S. Savo, B. D. F. Casse, S. Sridhar, Slow microwave waveguide made of negative permeability metamaterials. *Microwave Opt. Technol. Lett*. **51**, 2705–2709 (2009).

67. S. Savo, B. D. F. Casse, W. Lu, S. Sridhar, Observation of slow-light in a metamaterials waveguide at microwave frequencies. *Appl. Phys. Lett*. **98**, 171907 (2011).

68. I.-Y. Park *et al*., Plasmonic generation of ultrashort extreme ultraviolet light pulses. *Nature Photonics* **5**, 677-681 (2011).

69. K. L. Tsakmakidis *et al*., Breaking Lorentz reciprocity to overcome the time-bandwidth limit in physics and engineering. *Science* **356**, 1260-1264 (2017).

70. C. Ciracì *et al*., Probing the ultimate limits of plasmonic enhancement. *Science* **337**, 1072-1074 (2012).

71. J. A. Scholl, A. L. Koh, J. A. Dionne, Quantum plasmon resonances of individual metallic nanoparticles. *Nature* **483**, 421-427 (2012).

72. K. J. Savage *et al*., Revealing the quantum regime in tunnelling plasmonics. *Nature* **491**, 574-577 (2012).

73. S. Kim *et al*., High harmonic generation by resonant plasmon field enhancement. *Nature* **453**, 757–760 (2008).

74. M. Sivis, M. Duwe, B. Abel, C. Ropers, Nanostructure-enhanced atomic line emission. *Nature* **485**, E1-E3 (2012).

75. Q. Gan, Z. Fu, Y. J. Ding, F. J. Bartoli, Ultrawide-bandwidth slow-light system based on THz plasmonic graded metallic grating structures. *Phys. Rev. Lett*. **100**, 256803 (2008).

76. Q. Gan, Y. J. Ding, F. J. Bartoli, "Rainbow" trapping and releasing at telecommunication wavelengths. *Phys. Rev. Lett*. **102**, 056801 (2009).

77. Z. Fu, Q. Gan, Y. J. Ding, F. J. Bartoli, From waveguiding to spatial localization of THz waves within a plasmonic metallic grating. *IEEE Sel. Topics Quantum Electron*. **14**, 486–490 (2008).

78. L. Chen, G. P. Wang, Q. Gan, F. J. Bartoli, Trapping of surface-plasmon polaritons in a graded Bragg structure: Frequency-dependent spatially separated localization of the visible spectrum modes. *Phys. Rev. B* **80**, 161106(R) (2009).

79. V. N. Smolyaninova, I. I. Smolyaninov, A. V. Kildishev, V. M. Shalaev, Experimental observation of the trapped rainbow. *Appl. Phys. Lett*. **96**, 211121 (2010).

80. H. Choi, D. F. P. Pile, S. Nam, G. Bartal, X. Zhang, Compressing surface plasmons for nano-scale optical focusing. *Opt. Express* **17**, 7519 (2009).

81. X. P. Zhao *et al*., Trapped rainbow effect in visible light left-handed heterostructures. *Appl. Phys. Lett*. **95**, 071111 (2009).

82. V. Smolyaninova, I. Smolyaninov, A. Kildishev, V. M. Shalaev, Trapped rainbow techniques for spectroscopy on a chip and fluorescence enhancement. *Applied Physics B* **106**, 577-581 (2012).

83. A. I. Fernández-Domínguez, S. A. Maier, J. B. Pendry, Collection and concentration of light by touching spheres: A transformation optics approach. *Phys. Rev. Lett*. **105**, 266807 (2010).

84. Y. Luo, D. Y. Lei, S. A. Maier, J. B. Pendry, Broadband light harvesting nanostructures robust to edge bluntness. *Phys. Rev. Lett*. **108**, 023901 (2012).

85. Y. Luo, A. Aubry, J. B. Pendry, Electromagnetic contribution to surface-enhanced Raman scattering from rough metal surfaces: A transformation optics approach. *Phys. Rev. B* **83**, 155422 (2011).

86. A. C. Atre *et al*., Toward high-efficiency solar upconversion with plasmonic nanostructures. *J. Opt*. **14**, 024008 (2012).

87. Y. Lu *et al*., Nanophotonic crescent moon structures with sharp edge for ultrasensitive biomolecular detection by local electromagnetic field-enhancement effect. *Nano Lett*. **5**, 119-124 (2005).

88. K. Kneipp *et al*., Extremely large enhancement factors in surface-enhanced Raman scattering for molecules on colloidal gold clusters. *Applied Spectroscopy* **52**, 1493-1497 (1998).

89. Y. Cui *et al*., Ultrabroadband light absorption by a sawtooth anisotropic metamaterial slab. *Nano Lett*. **12**, 1443-1447 (2012).

90. S.-H. Gong *et al*., Self-aligned deterministic coupling of single quantum emitter to nanofocused plasmonic modes. *Proc. Nat. Acad. Sciences USA* **112**, 5280-5285 (2015).

91. O. Hess, K. L. Tsakmakidis, Metamaterials with quantum gain. *Science* **339**, 654-655 (2013).

92. K. L. Tsakmakidis *et al*., Plasmonic nanolasers without cavity, threshold and diffraction limit using stopped light, in *Frontiers in Optics 2012* (Rochester, New York, USA, 2012), paper FTh2A.2.

93. T. Pickering, J. M. Hamm, A. F. Page, S. Wuestner, O. Hess, Cavity-free plasmonic nanolasing enabled by dispersionless stopped light. *Nature Commun*. **5**, 4972 (2014).

94. S. Wuestner, T. Pickering, J. M. Hamm, A. F. Page, A. Pusch, O. Hess, Ultrafast dynamics of nanoplasmonic stopped-light lasing. *Faraday Discuss*. **178**, 307-324 (2015).

95. H. Choo *et al*., Nanofocusing in a metal-insulator-metal gap plasmon waveguide with a three-dimensional linear taper. *Nature Photon*. **6**, 838-844 (2012).

96. A. Melikyan *et al*., High-speed plasmonic phase modulators. *Nature Photon*. **8**, 229-233 (2014).

97. Q. Gan, Y. Gao, K. Wagner, D. Vezenov, Y. J. Ding, F. J. Bartoli, Experimental verification of the rainbow trapping effect in adiabatic plasmonic gratings. *Proc. Natl. Acad. Sci. USA* **108**, 5169–5173 (2011).

98. Z. H. Fang *et al*., Slowing down light using a dendritic cell cluster metasurface waveguide. *Sci. Rep*. **6**, DOI: 10.1038/srep37856 (2016).

99. E. Laux, C. Genet, T. Skauli, T. W. Ebbesen, Plasmonic photon sorters for spectral and polarimetric imaging. *Nature Photonics* **2**, 161-164 (2008).

100. M. H. Kryder *et al*., Heat assisted magnetic recording. *Proc. IEEE* **96**, 1810-1835 (2008).

101. W. A. Challener *et al*., Heat-assisted magnetic recording by a near-field transducer with efficient optical energy transfer. *Nature Photon*. **3**, 220-224 (2009).

102. C. W. J. Beenakker, R. A. Sepkhanov, A. R. Akhmerov, J. Tworzydło, Quantum Goos-Hänchen effect in graphene. *Phys. Rev. Lett*. **102**, 146804 (2009).

103. L. Zhao, S. F. Yelin, Proposal for graphene-based coherent buffers and memories. *Phys. Rev. B* **81**, 115441 (2010).

104. A. Woessner *et al*., Highly confined low-loss plasmons in graphene-boron nitride heterostructures. *Nature Materials* **14**, 421-425 (2015).

105. A. K. Geim, I. V. Grigorieva, Van der Waals heterostructures. *Nature* **499**, 419-425 (2013).

106. A. Poddubny, I. Iorsh, P. Belov, Y. Kivshar, Hyperbolic metamaterials. *Nature Photonics* **7**, 948-957 (2013).

107. S. Dai *et al*., Graphene on hexagonal boron nitride as a tunable hyperbolic metamaterial. *Nature Nanotechnol*. **10**, 682-686 (2015).

108. M. Gullans, D. Chang, F. H. L. Koppens, F. J. García de Abajo, M. Lukin, Single-photon nonlinear optics with graphene plasmons. *Phys. Rev. Lett*. **111**, 247401 (2013).

109. S. Dai *et al*., Tunable phonon polaritons in atomically thin van der Waals crystals of boron nitride. *Science* **343**, 1125-1129 (2014).

110. E. Yoxall *et al*., Direct observation of ultraslow hyperbolic polariton propagation with negative phase velocity. *Nature Photon*. **9**, 674-678 (2015).

111. A. Giugni *et al*., Hot-electron nanoscopy using adiabatic compression of surface plasmons. *Nature Nanotech*. **8**, 845-852 (2013).

112. M. Sandtke, L. Kuipers, Slow guided surface plasmons at telecom frequencies. *Nature Photonics* **1**, 573-576 (2007)

113. A. C. Atre *et al*., Nanoscale optical tomography with cathodoluminescence spectroscopy. *Nature Nanotech*. **10**, 429-436 (2015).

114. R. El-Ganainy, K. G. Makris, D. N. Christodoulides, Z. H. Musslimani, Theory of coupled optical PT-symmetric structures. *Opt. Lett*. **32**, 2632-2634 (2007).

115. C. Wu, A. B. Khanikaev, G. Shvets, Broadband slow-light metamaterial based on a double-continuum Fano resonance. *Phys. Rev. Lett*. **106**, 107403 (2011).

116. R. Yang, W. Zhu, J. Li, Realization of "trapped rainbow" in 1D slab waveguide with surface dispersion engineering. *Opt. Express* **23**, 6326-6335 (2015).

117. N. Yu, F. Capasso, Flat optics with designer metasurfaces. *Nature Materials* **13**, 139-150 (2014).

118. A. V. Kildishev, A. Boltasseva, V. M. Shalaev, Planar photonics with metasurfaces. *Science* **339**, 1232009 (2013).
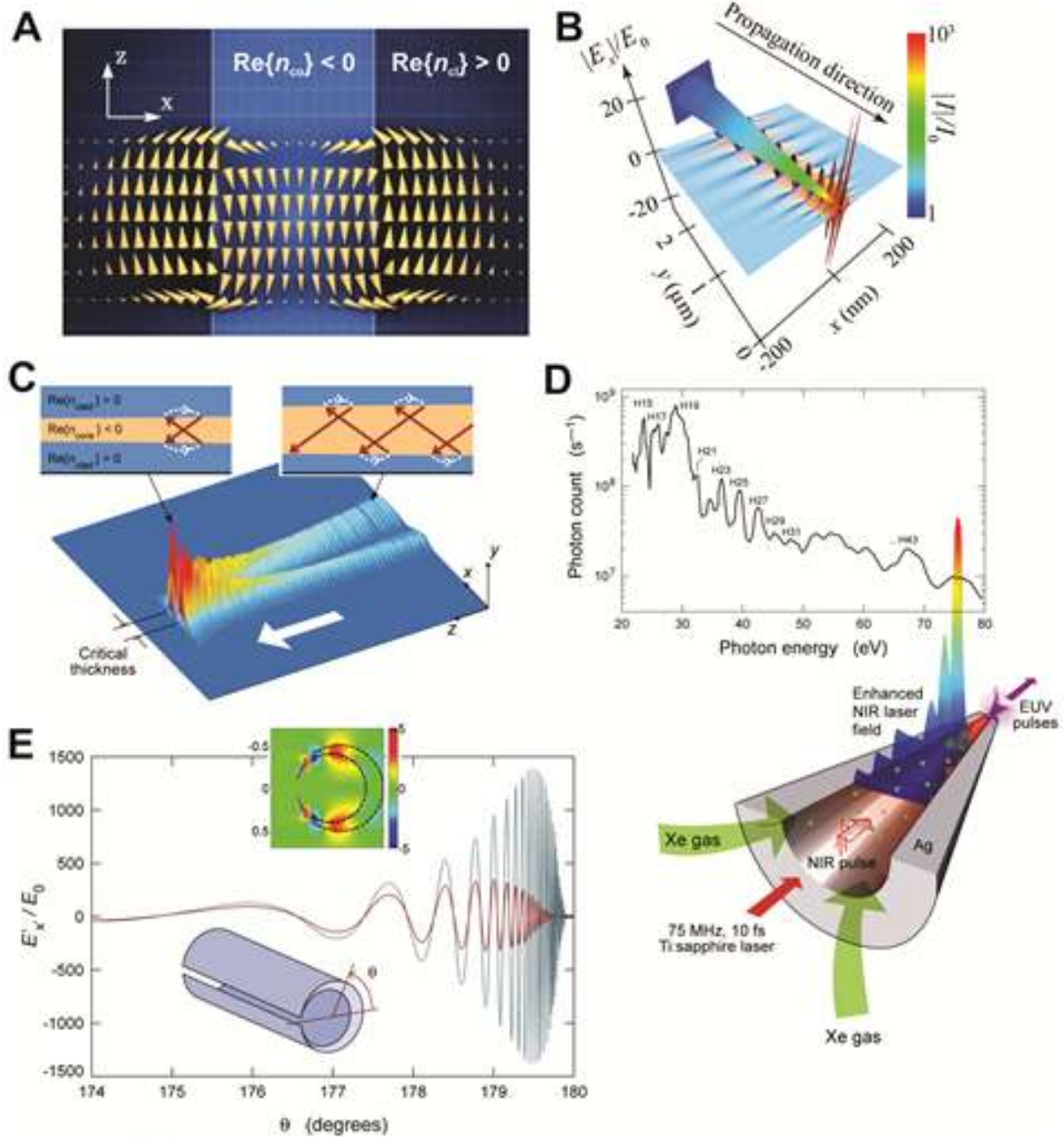
Fig. 1. Broadband ultraslow light in metamaterials and nanoplasmonics. (**A**) Structure of the Poynting vector field in a symmetric waveguide made of a negative-refractive-index core layer and positive-index claddings, showing the opposite directions of the power flux in the core ($P_{co} < 0$) and cladding ($P_{cl} > 0$) layers. Owing to the characteristic double-vortex structure of the power flux, the total time-averaged power flow in the $+z$ direction ($P_{tot} = P_{co} + P_{cl}$) is reduced, leading to correspondingly reduced energy and group velocities (*39*). (**B**) Adiabatic nanofocusing of surface plasmon polaritons (SPPs) guided along a tapered plasmonic nanoguide. The group velocity of the SPPs progressively reduces as they propagate, becoming zero at the nanostructure's tip, thereby leading to significant spatial compression in the longitudinal direction and to a correspondingly large local field enhancement (here, of the order of ~10^3) (*40*). (**C**) Snapshot of the propagation of a monochromatic lightwave along an adiabatically tapered waveguide with negative-refractive-index core and positive-refractive-index claddings. The lightwave progressively slows-down until it stops at a "critical" thickness, where the electric field builds up. The top-right and top-left insets associate the wave propagation with the

corresponding zigzag ray picture at different guide widths. Note the *negative* Goos-Hänchen phase-shifts (denoted with dotted white arrows) each time the ray hits an interface (*42*). (**D**) (lower panel) A near-infrared (NIR, ~ 800 nm) surface-plasmon polariton (SPP) propagating along a tapered conical plasmonic nanoguide, after being excited by a NIR laser pulse. The SPP slows-down while propagating towards the exit aperture, where it eventually converges to a sub-wavelength high-intensity local spot. The hollow plasmonic (Ag) nanoguide is filled with xenon atoms, which are ionised by the high-intensity local field, producing high-harmonic EUV pulses that are radiated through the exit aperture. The upper panel shows the measured high-harmonic-generation spectrum, spanning from the fifteenth to the forty-third harmonic (*68*). (**E**) Slow SPPs propagating azimuthally (in the **θ** direction) towards the singular ("kissing") point of the crescent nanostructure shown in the inset, after being excited by a plane wave. Shown is the amplitude of the *x*-component of the electric field at an arbitrary 2D cross-section of the nanocrescent. Note that the field-enhancement peaks at an angle other than 180°. The upper inset shows a cross-sectional plot of the amplitude of the *x*-component of the electric field normalized by the incident field (polarized along *x*). The colour scale in this inset is linear and restricted to [-5 5], but it should be noted that the field magnitude is by far larger around the singularity ("kissing point") of the two touching cylinders, as shown in the main figure (*64*).
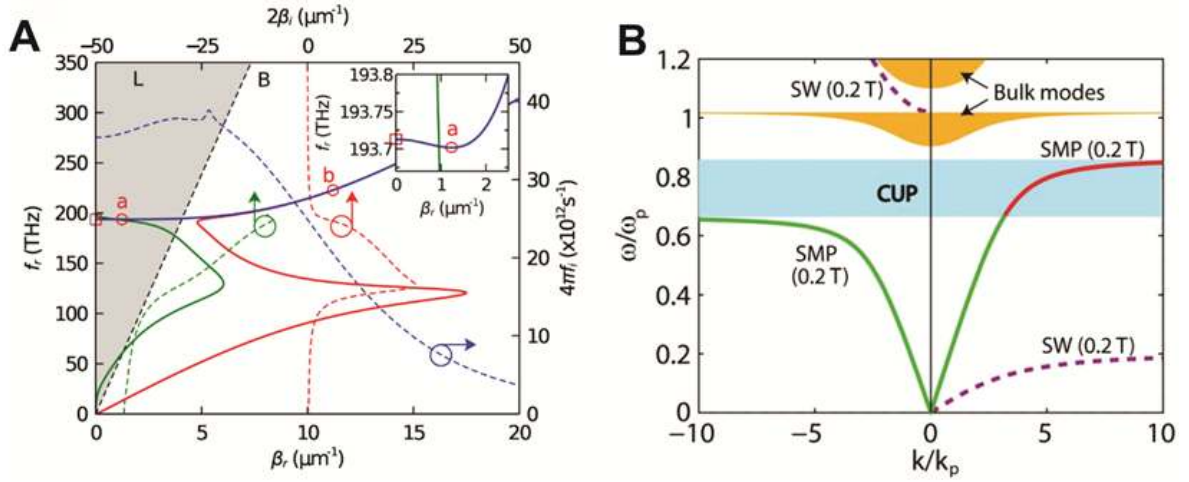
Fig. 2. Robust stopped light in the presence of absorption and scattering channels. In both (**A**) and (**B**) the displayed results have been obtained based on exact, analytic solutions of Maxwell's equations. (**A**) Dispersion diagram of the two classes of complex TM_2 modes, complex-ω (blue) and complex-β (red and green), supported by a lossy plasmonic (ITO)–silicon–plasmonic (ITO) planar waveguiding heterostructure. Solid lines show the real part of the frequency [$f_r = \text{Re}\{\omega\}/(2\pi)$] and of the longitudinal propagation constant ($\beta_r = \text{Re}\{\beta\}$), while the dashed lines show the corresponding imaginary parts ($f_i = \text{Im}\{\omega\}/(2\pi)$, $\beta_i = \text{Im}\{\beta\}$). The imaginary part of the frequency, f_i, provides the temporal losses associated with the complex-ω mode, while the imaginary part of the propagation constant, β_i, provides the spatial losses associated with the two complex-β modes. Note how only the complex-ω mode retains a zero group velocity, at point "a", where the band's slope locally becomes zero (see inset). The shaded grey region indicates the free-space light cone (*38*). (**B**) Band diagram of a gyroelectric-semiconductor (InSb)–silicon–plasmonic (Ag) heterostructure for the case where an external magnetic field $B_0 = 0.2$ T is applied in a direction perpendicular to the structure. Shown are, both for positive and negative longitudinal wavevectors k, the dispersion curve of the supported semiconductor–dielectric–metal surface magnetoplasmon (SMP), the surface wave at an InSb/Ag interface (SW), and the region of the bulk modes in InSb. The area shaded in cyan indicates the band region where complete unidirectional propagation (CUP) of the supported surface magnetoplasmon is attained (*69*).
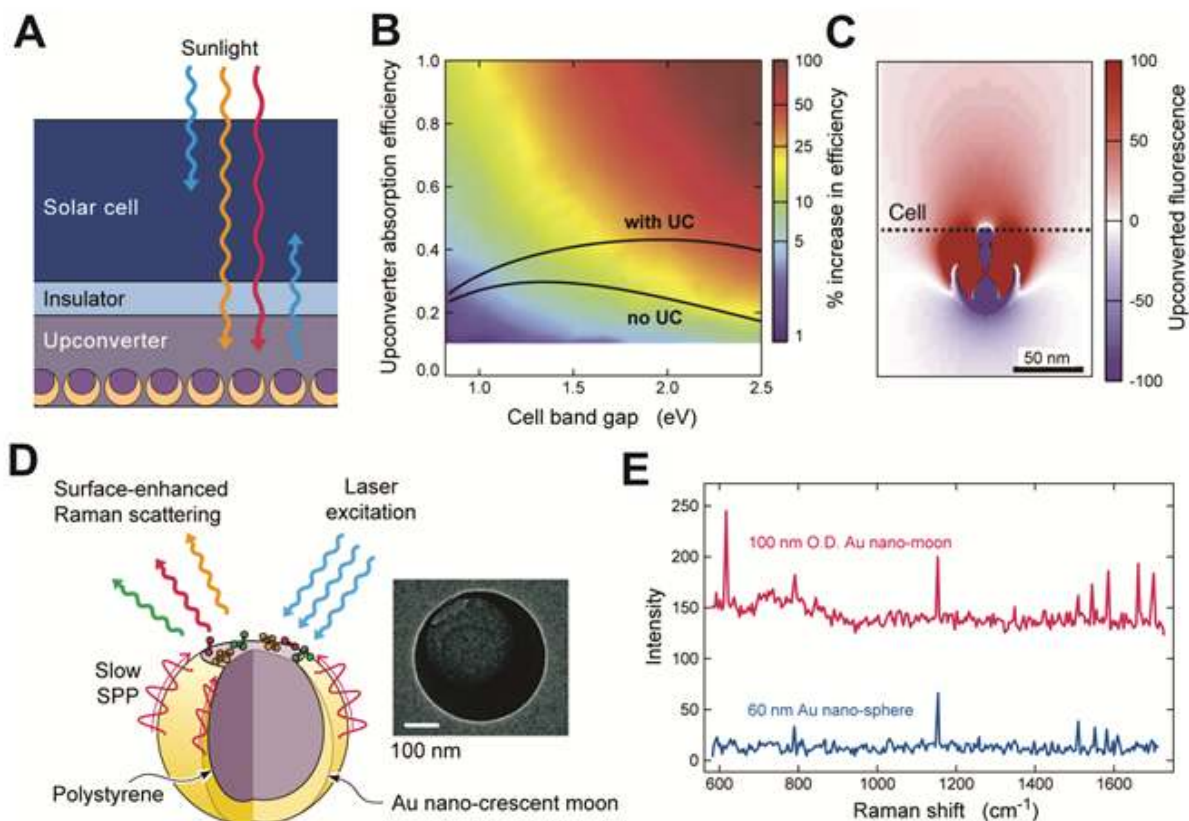
Fig. 3. Broadband ultraslow light at the meta-atomic level, and its application in photovoltaics and bio-sensing. (**A**) Schematic illustration of a solar-cell based on an upconverter system where above-bandgap light is absorbed by the cell, while sub-bandgap light is initially absorbed in the upconverter layer, converted to above-bandgap light, and sent back to the cell where it is harvested. The upconverter consists of slow-light nanocrescent meta-atoms, whose core is doped with the upconverting material (*86*). (**B**) The upconverter significantly increases the efficiency of an ideal single-junction solar cell. As shown here, the relative increase is greatest when the upconverter absorption efficiency and the cell bandgap are high. The black-line inset shows the absolute efficiency of an ideal solar cell, both with and without an ideal upconverter (UC) (*86*). (**C**) Calculation of the upconverted power towards the solar cell (in W/m^2). At a wavelength of 644 nm, the herein shown power flow into the cell is enhanced by more than 100 times compared with the case (not shown here) where there is no crescent in the upconverter (*86*). (**D**) Conceptual illustration of a SERS substrate made of broadband slow-light nanocrescent moons. The gold surface is functionalized with biomolecular linkers to recognize specific biomolecules. Also shown at the right part is a transmission electron microscope image of an actual nanocrescent moon. The nanocrescent moon have an inner diameter of 300 nm and a bottom thickness of 100 nm (*87*). (**E**) Comparison between the SERS spectra of 1 mM R6G molecules sitting on top of the slow-light nanocrescent moons and on 60 nm standard colloidal Au nanospheres (*87*).
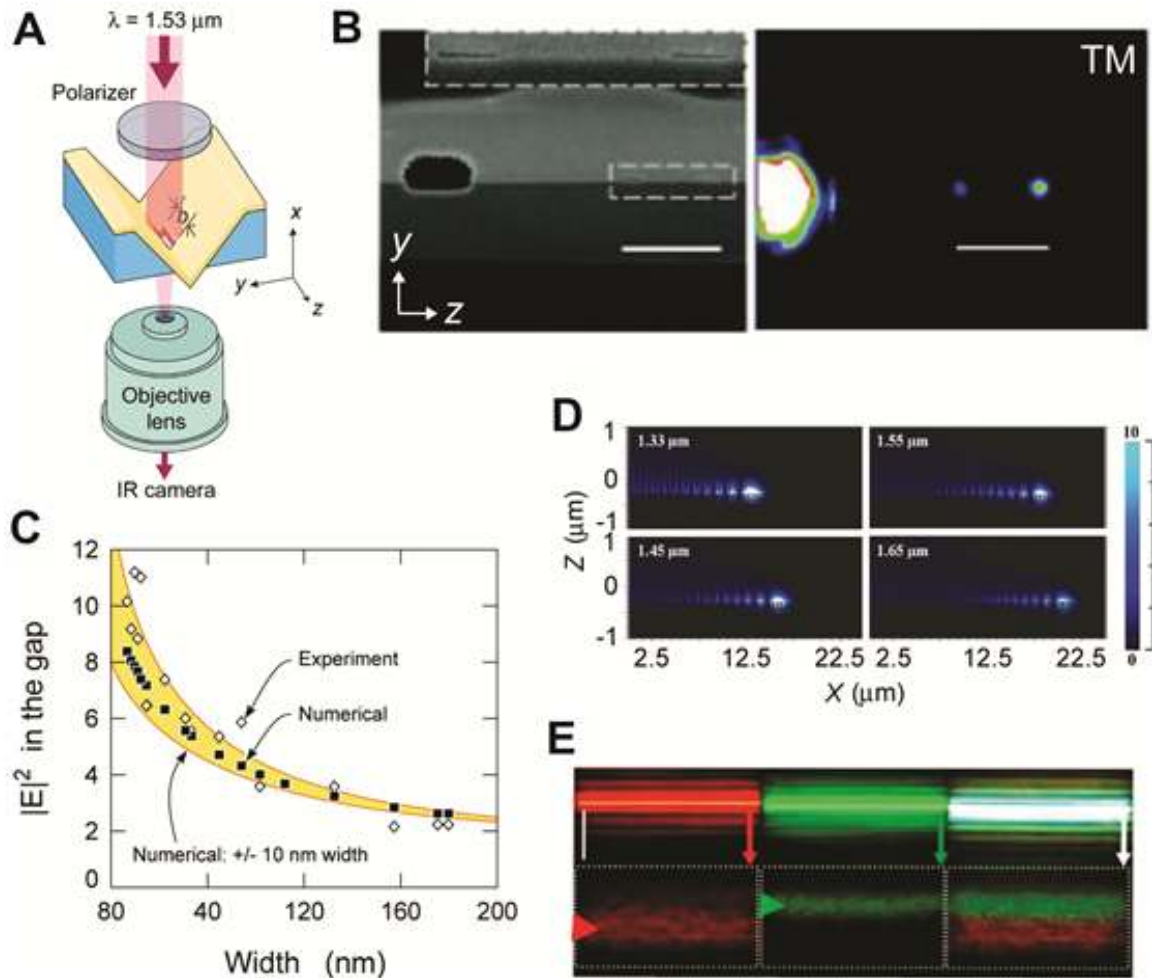
Fig. 4. Broadband slow, conventional and "spoof", surface plasmon polaritons, and their application in spectrum demultiplexing and colour sorting. (**A**) Schematic illustration of the experimental setup used for slowing and bringing to the nanoscale TM-polarized light (magnetic field parallel to z-axis). The incident vacuum wavelength was 1532 nm (*80*). (**B**) (left) An SEM image of two subwavelength-width (~ 100 nm) V-groove output slits and a large reference hole as seen from the back side (along x). (right) Output signal for TM polarization of the incident lightfield. When the incident-light polarization is TE, no plasmon mode is excited at the two subwavelength slits (*80*). (**C**) Dependence of intensity ($|E|^2$) enhancement with the width of the V-groove slit, as determined experimentally and numerically (*80*). (**D**) Numerical simulations of slow "spoof" SPPs propagating along a tapered plasmonic grating. SPPs of broadly different frequencies (in the telecommunications regime) are stopped and trapped at correspondingly different points along the nanoguide (*76*). (**E**) Experimental demonstration, at visible frequencies, of the scheme in **D**. Here, visible light of different colours is incident on a nanoslit from the bottom of the structure (the nanoslit extends horizontally, and is perpendicular to the arrows at their starting points), acquiring enough momentum to couple to spoof SPPs. The so-excited SPPs propagate slowly in the direction indicated by the arrows along the tapered grating (shown here from above), with each colour eventually being stopped and trapped at a different groove depth ("rainbow trapping"). The white scale bar shown in the top left panel corresponds to 10 µm (*97*).
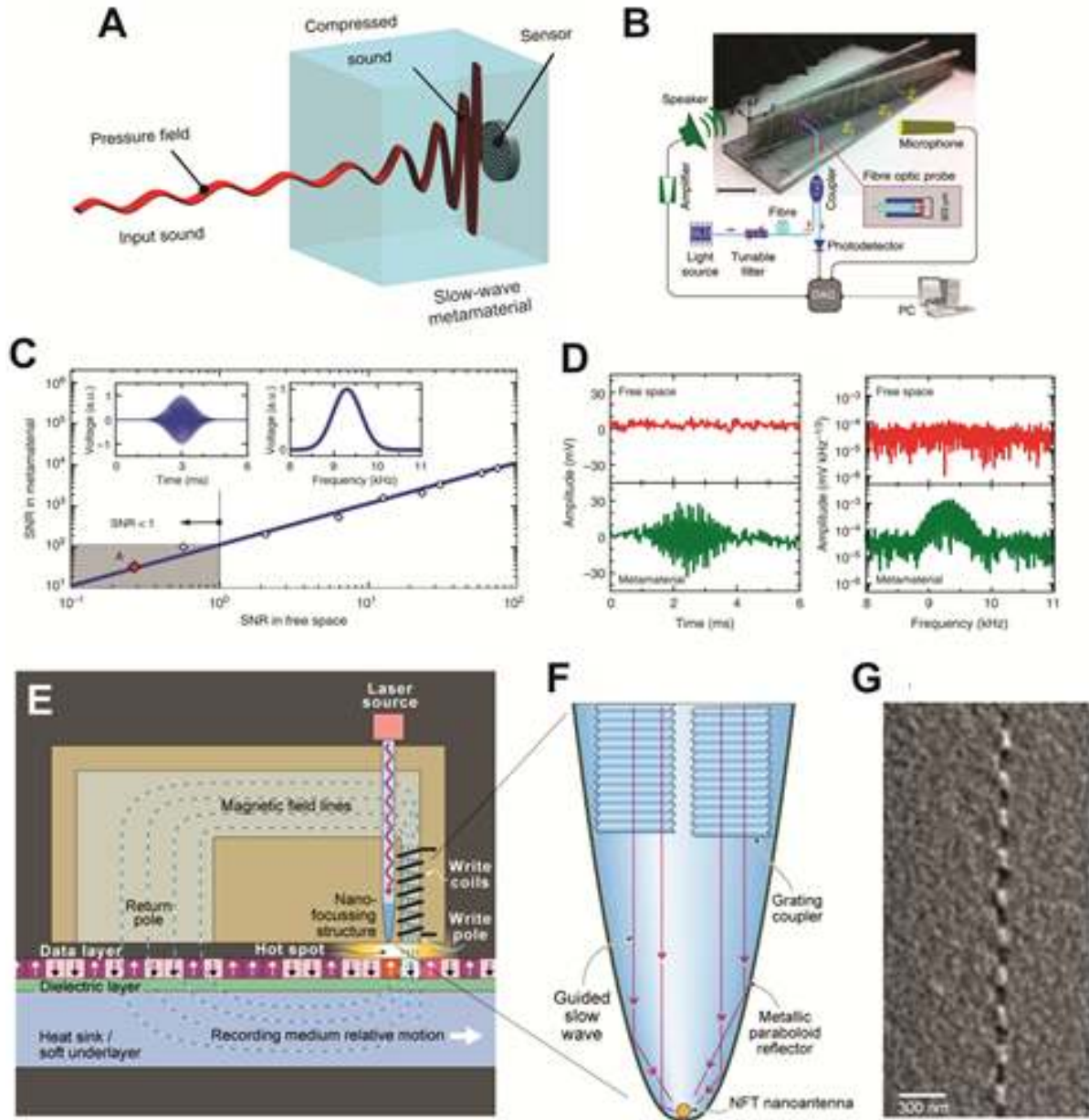
Fig. 5. Adiabatic wave slowing-down and focusing for enhanced acoustic sensing and nanooptical heat-assisted magnetic recording (HAMR). (**A**) Schematic of how the pressure-field of a sound wave is spatially compressed and enhanced while decelerated inside an acoustic metamaterial, before being detected by a sensor (*61*). (**B**) Photonic-acoustic metamaterial hybrid sensing system. The device is constructed from an array of stainless plates, spaced by air gaps, and has a progressively increased width (*61*). (**C**) The signal-to-noise ratio (SNR) measured in the metamaterial compared with that obtained in free space. The inset shows the input Gaussian pulses from the speaker in time domain (left) and frequency domain (right). The diamond dots are the experimental data and the solid line is the fitted curve with a slope of 114, indicating an approximately 20 dB SNR improvement by using the ultraslow-acoustic-wave-enhanced sensing system. In the grey highlighted zone, the measured free-space SNR is smaller than one, indicating that the input signal is below the detection limit (*61*). (**D**) Time-domain and frequency-domain pulse signal measured in free space (top) and in the metamaterial (bottom). The SNR measured in the metamaterial device is 32.7, compared with the measured free-space SNR of 0.27, which corresponds to point A in **C** (*61*). (**E**) A HAMR head records data to a disk medium of high thermal stability. Here, a guided wave excited by a laser source propagates slowly along a parabolically-tapered metal-clad waveguide (shown in **F**), adiabatically stopping and focusing at the cutoff-tip of the guide, and eventually coupling to an astutely shaped plasmonic nanoparticle (nanoantenna). The wave's

23

adiabatic slowing and stopping is similar to that shown in Fig. 1, B to E, and Fig. 3, A and D, but now for a parabolic taper. The resulting high-intensity local field is used to heat the recoding medium locally, assisting the recording process by temporarily lowering its resistance to magnetic polarization (*101*). (**F**) Schematic illustration (not to scale) of a side view of the HAMR recording head. In the upper part of the recording head there is a grating, coupling laser-diode light to the parabolically-tapered metal-clad optical waveguide. At the bottom of the tip there is a plasmonic nanoantenna ("near-field transducer", NFT) on which light energy is evanescently coupled (red arrows) (*101*). (**G**) Magnetic force microscope image of a recorded track. The track width is ∼70 nm (scale bar, 300 nm) (*101*).
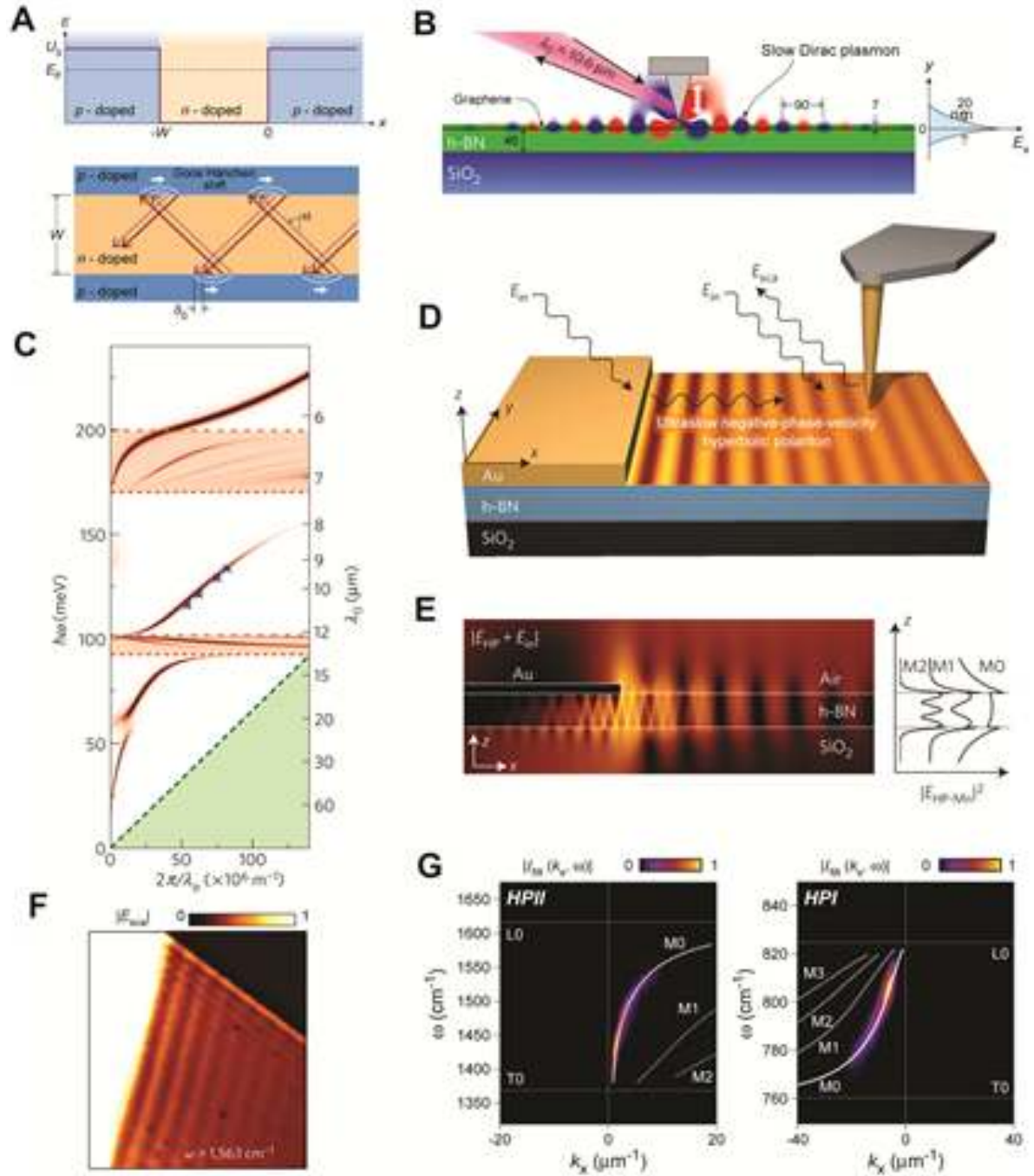
Fig. 6. Broadband ultraslow guided Dirac electrons, plasmons and phonon-polaritons in graphene, van der Waal crystals and heterostructures. (**A**) (upper part) Potential profile of an *n*-doped graphene, bounded symmetrically by two *p*-doped regions. (lower part) Illustration of the reflections of the two pseudospin Dirac-electron components at the two *p-n* interfaces, along with the associated *negative* quantum Goos-Hänchen phase shifts. The two zigzag-propagating rays, shown in red and purple, trace the movement of the centre of a guided slow electron beam on the two graphene sublattices (*102*). (**B**) Schematic of graphene encapsulated by h-BN, and the associated s-SNOM measurement setup for the excitation of a guided slow Dirac plasmon. The simulated E_x field-component of the plasmon in the out-of-plane direction (20 nm full-width at half-maximum) can be seen on the right (*104*). (**C**) Calculated dispersion diagram of the slow Dirac plasmons of **B**, for a carrier density of $n_s = 7.4 \times 10^{12}$ cm^{-2}. The crosses show experimental data, while the shadowed regions show the h-BN frequency bands where propagating phonon polaritons can exist (shaded orange) and the electronic intraband Landau damping region (shaded green). The red background colour shows the

imaginary part of the reflection coefficient of evanescent waves, evaluated at the top h-BN surface using the transfer-matrix method for a vacuum–SiO$_2$(285 nm)–h-BN(46 nm)–graphene–h-BN(7 nm)–vacuum heterostructure (with the dips in the reflection coefficient coinciding with the excited modes in the heterostructure) (*104*). (**D**) Schematic of structure and the setup for exciting and observing ultraslow negative-phase-velocity hyperbolic phonon polaritons in a thin h-BN slab. The polaritons are launched with the aid of the metal (Au) edge, and the thickness of the h-BN layer is 135 nm. Type I polaritons are found in the spectral region 22.8 THz (13.6 μm) - 24.7 THz (12.1 μm), whereas Type II polaritons exists between 41.1 THz (7.3 μm) - 48.3 THz (6.2 μm) (*110*). (**E**) (left) Numerical calculation of the field distribution (on a log scale) for the structure of **D**, at ω = 1563 cm^{-1} (46.9 THz; 6.4 μm). The propagation of the type-II fundamental hyperbolic polariton mode is also shown here as rays propagating in a zig-zag fashion along the slab, being reflected from the top and bottom media interfaces – similarly to the zig-zag ray propagation that was shown before in Fig. 1C (although here the phase velocity of the type-II mode is positive and the Goos-Hänchen phase shifts are not clearly discerned). (right) Field-intensity profiles of the first three guided hyperbolic slow modes (*110*). (**F**) Infrared near-field image of the interference between the polaritons launched by the gold edge and those by the tip (see **D**) upon being reflected by the h-BN edge (*110*). (**G**) Comparison between the experimentally (colour) and numerically (white solid) determined dispersion curves of the fundamental type-II (left) and type-I (right) hyperbolic polariton mode. The white dashed lines show numerically calculated higher-order guided modes (*110*).